

Article

Open Access

Crystal plane engineering of MAPbI₃ in epoxy-based materials for superior gamma-ray shielding performance

Kai Cui¹, Yang Li^{1,*}, Wenjing Wei¹, Qianqian Teng¹, Tianyu Zhang¹, Jinzhu Wu¹, Hongjun Kang¹, Wei Qin^{2,*} and Xiaohong Wu^{1,*}

Abstract

The rapid development of the aerospace and nuclear industries is accompanied by increased exposure to high-energy ionising radiation. Thus, the performance of radiation shielding materials needs to be improved to extend the service life of detectors and ensure the safety of personnel. The development of novel lightweight materials with high electron density has therefore become urgent to alleviate radiation risks. In this work, new MAPbI₃/epoxy (CH₃NH₃PbI₃/epoxy) composites were prepared via a crystal plane engineering strategy. These composites delivered excellent radiation shielding performance against 59.5 keV gamma rays. A high linear attenuation coefficient (1.887 cm⁻¹) and mass attenuation coefficient (1.352 cm² g⁻¹) were achieved for a representative MAPbI₃/epoxy composite, which was 10 times higher than that of the epoxy. Theoretical calculations indicate that the electron density of MAPbI₃/epoxy composites significantly increases when the content ratio of the (110) plane in MAPbI₃ increases. As a result, the chances of collision between the incident gamma rays and electrons in the MAPbI₃/epoxy composites were enhanced. The present work provides a novel strategy for designing and developing high-efficiency radiation shielding materials.

Keywords: Perovskite, Gamma-ray shielding, Electron density, Crystal plane engineering

Introduction

As deep-space exploration enters a new era, the requirements for the service life and performance of detectors on spacecraft are becoming more stringent^{1,2}. In the space environment, various types of ionising radiation can damage the detectors on the spacecraft³. Furthermore, in the nuclear industry and the field of nuclear medicine, similar radiation damage could cause health problems for

personnel, including dizziness, fatigue, loss of appetite, hair loss, and other adverse reactions⁴⁻⁶. An urgent need to alleviate these radiation risks has therefore arisen.

The key approach to mitigating radiation risks is to shorten the exposure time to the radiation source, increase the distance from the radiation source, and use shielding materials⁷. Among these, the application of shielding materials is the most effective method. Short-wavelength X-rays and γ -rays are typical forms of high-energy ionising radiation with strong penetration ability⁸. The most commonly used X/ γ -ray shielding materials are those with high atomic numbers (*Z*), such as lead, tungsten, tantalum, and concrete, but their high density hinders their commercial application^{9,10}. Hence, it is necessary to

Correspondence: Yang Li (liyong198517@hit.edu.cn) or Wei Qin (qinwei@hit.edu.cn) or Xiaohong Wu (wuxiaohong@hit.edu.cn)

¹School of Chemistry and Chemical Engineering, Harbin Institute of Technology, Harbin, Heilongjiang 150001, China

²School of Materials Science and Engineering, Harbin Institute of Technology, Harbin, Heilongjiang 150001, China

© The Author(s) 2022



Open Access This article is licensed under a Creative Commons Attribution 4.0 International License, which permits use, sharing, adaptation, distribution and reproduction in any medium or format, as long as you give appropriate credit to the original author(s) and the source, provide a link to the Creative Commons license, and indicate if changes were made. The images or other third party material in this article are included in the article's Creative Commons license, unless indicated otherwise in a credit line to the material. If material is not included in the article's Creative Commons license and your intended use is not permitted by statutory regulation or exceeds the permitted use, you will need to obtain permission directly from the copyright holder.

To view a copy of this license, visit <http://creativecommons.org/licenses/by/4.0/>.

develop alternative lightweight materials with excellent radiation shielding performance.

Certain polymers and their composites have been shown to be promising alternatives to lead and concrete as radiation shielding materials because they are lightweight and flexible with excellent physical, mechanical, and radiation resistance properties^{11,12}. In the past few years, several studies have concluded that fillers in composites play a crucial role in their radiation shielding performance^{13–15}. El-Khatib et al. studied the effects of the size of CdO particles on the gamma-ray shielding performance of CdO/HDPE, showing that the collision between gamma rays and CdO particles is dependent on the particle sizes¹⁶. This suggests that the development and design of novel fillers would be an effective strategy for improving the radiation shielding performance.

Organic-inorganic hybrid perovskites have been widely used in photoelectric devices and radiation detectors owing to their high absorption coefficient, long carrier diffusion length, low cost, lightness, and flexibility^{17–20}. Chen et al. prepared a series of unique inorganic perovskite nanocrystals composed of caesium and lead and found that the scintillator characteristics of these perovskites facilitate their interaction with high-energy photons (i.e. X-rays and γ -rays)²¹. Therefore, organic-inorganic hybrid perovskites have potential as fillers in radiation-shielding materials. However, to the best of our knowledge, the fabrication of perovskite/polymer composites for radiation shielding has not been reported previously.

In this work, we prepared MAPbI₃ microcubic crystals by a simple solvothermal method and then fabricated MAPbI₃/epoxy composites. The gamma-ray shielding performance of MAPbI₃/epoxy composites was evaluated using an Am-241 source. The results showed that MAPbI₃ with altered crystal planes plays a determining role in the gamma-ray shielding performance of the corresponding composites. The best linear and mass attenuation coefficients obtained for the MAPbI₃/epoxy composite were 1.887 cm⁻¹ and 1.352 cm² g⁻¹, respectively. The present work provides essential guidelines for the design and synthesis of high-efficiency radiation-shielding composites.

Results

Synthesis of the MAPbI₃ microcubic crystals

MAPbI₃ microcubic crystals were directly synthesised by a facile one-step solvothermal process and then mixed with epoxy to fabricate MAPbI₃/epoxy composites (Fig. 1a). To understand the correlation between the reaction time (T_{reaction}) and crystal structure of MAPbI₃, a series of reaction times (i.e. 0.5, 1.0, 1.5, 2.0, and 2.5 h) were used. The reaction time was found to play a considerable role in tailoring the crystal planes of the MAPbI₃ microcubic crystals. Prolongation of the reaction time had the effect of increasing the content ratio of the (110) crystal plane to the (220) crystal plane, as shown in Fig. 1a. As shown in Fig. 1b–e, the SEM (scanning

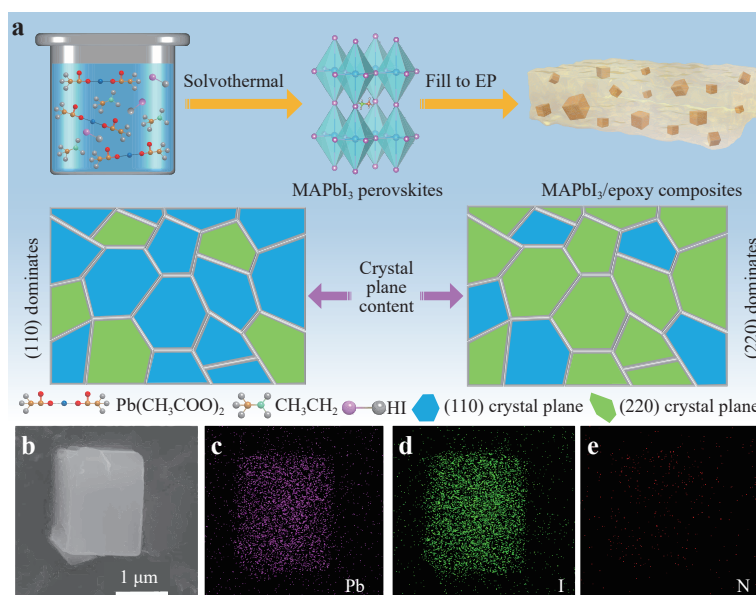


Fig. 1 Design scheme and morphology characterisation. **a** Schematic illustration of the MAPbI₃ microcubic crystals and the MAPbI₃/epoxy composites. **b** SEM image of MAPbI₃. **c–e** EDS mapping of Pb, I, and N, respectively.

electron microscope) and corresponding EDS (energy dispersive spectrometry) images of the MAPbI₃ microcubic crystals demonstrate an even and dense distribution of the elements Pb and I, together with a sparse distribution of the element N of MAPbI₃.

The surface composition and chemical states of the MAPbI₃ microcubic crystals were probed by X-ray photoelectron spectroscopy (XPS). The XPS survey spectrum shown in Fig. 2a indicates the presence of C, N, Pb, and I in a representative MAPbI₃ microcubic crystal. The corresponding high-resolution Pb 4f spectrum (Fig. 2b) presents two peaks at 137.6 eV and 142.4 eV, which are attributed to Pb 4f_{7/2} and Pb 4f_{5/2}, respectively²². In addition, the high-resolution I 3d spectrum (Fig. 2c) has two peaks located at 618.4 eV and 629.9 eV, ascribed to I 3d_{5/2} and I 3d_{3/2}, respectively²³. These results revealed that the MAPbI₃ microcubic crystals were successfully synthesised.

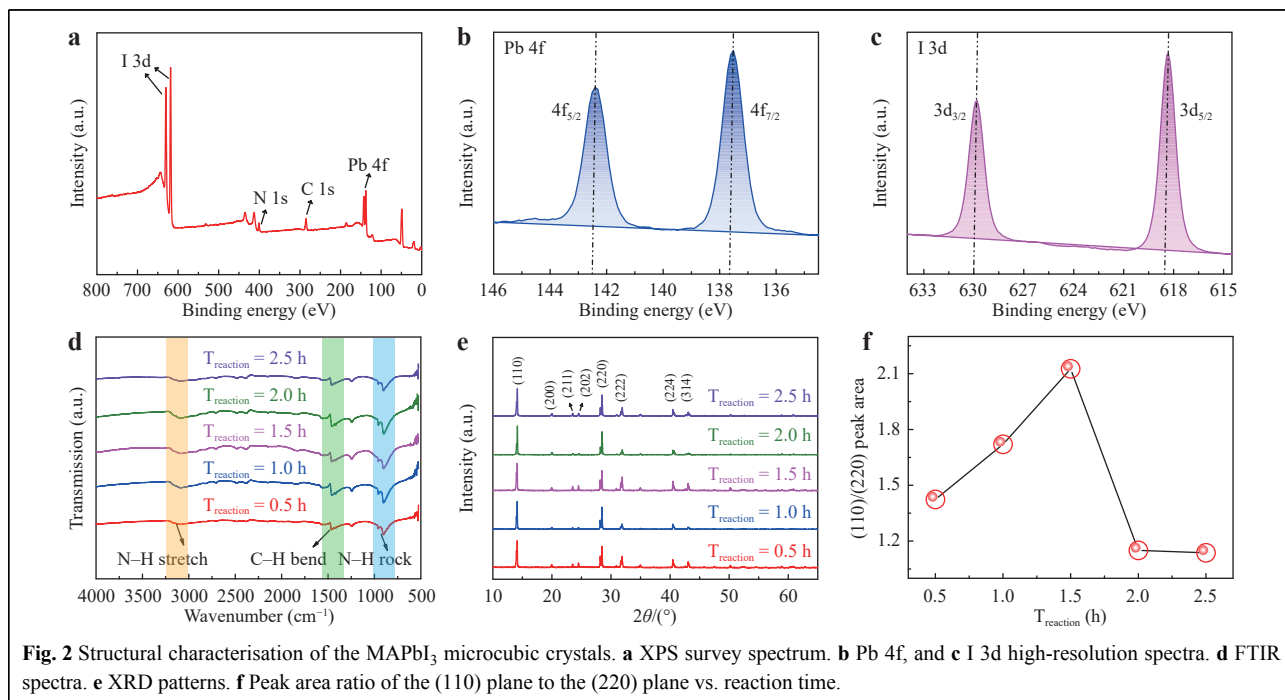
Fourier-transform infrared spectroscopy (FTIR) was used to determine the molecular structures of the MAPbI₃ microcubic crystals synthesised with different reaction times, as shown in Fig. 2d. The series of bands was identified as follows: (1) the band at 3132 cm⁻¹ is attributed to the N-H symmetric stretching mode, (2) the band at 1577 cm⁻¹ represents the C-H bending mode, and (3) the band at 911 cm⁻¹ represents the N-H rocking mode²⁴. These bands were not noticeably dependent on the reaction time, indicating that the molecular structures of the MAPbI₃ microcubic crystals prepared using different reaction times

were almost the same.

The phase structures of MAPbI₃ microcubic crystals were investigated using powder X-ray diffraction (XRD). The XRD patterns of MAPbI₃ microcubic crystals synthesised with reaction times of 0.5, 1.0, 1.5, 2.0, 2.5 h are shown in Fig. 2e. The diffraction peaks at 14.2°, 20.1°, 23.5°, 24.2°, 28.5°, 31.8°, 40.5°, and 43.1° correspond to the (110), (200), (211), (202), (220), (222), (224), and (314) planes of MAPbI₃ perovskite (tetragonal, space group=I4/mcm, a=b=8.8743 Å, c =12.6708 Å), which is consistent with previous reports²⁴. In addition, no diffraction peaks of other impurities such as PbI₂ were observed, indicating that the MAPbI₃ microcubic crystals prepared by the one-step solvothermal method are very pure.

Furthermore, the ratios of the peak areas of the (110) and (220) planes were compared, as shown in Fig. 2f, and these results show that the major crystal planes of the MAPbI₃ microcubic crystals vary with the reaction time. The ratio of the peak area of the (110) plane to that of the (220) plane increases with the reaction time from 0.5 h to 1.5 h, suggesting that the (110) plane is the dominant crystal plane in the MAPbI₃ microcubic crystal^{25,26}. However, a further increase in the reaction time to 2.5 h causes the peak of the (110) plane to become relatively less intense than that of the (220) plane. The results suggest that the reaction time plays a critical role in regulating the crystal planes of the MAPbI₃ microcubic crystals.

The HRTEM images (Fig. S1) further confirmed that the



MAPbI₃ microcubic crystals grew preferentially along the (110) and (220) planes²⁷. The FWHM of the (110) crystal plane reached its maximum value (Fig. S2) for a reaction time of 1.5 h, and the mean particle size of the MAPbI₃ microcubic crystals, as shown in the SEM image (Fig. S3), was measured as approximately 0.71 μm .

Gamma-ray shielding performance of the MAPbI₃/epoxy composites

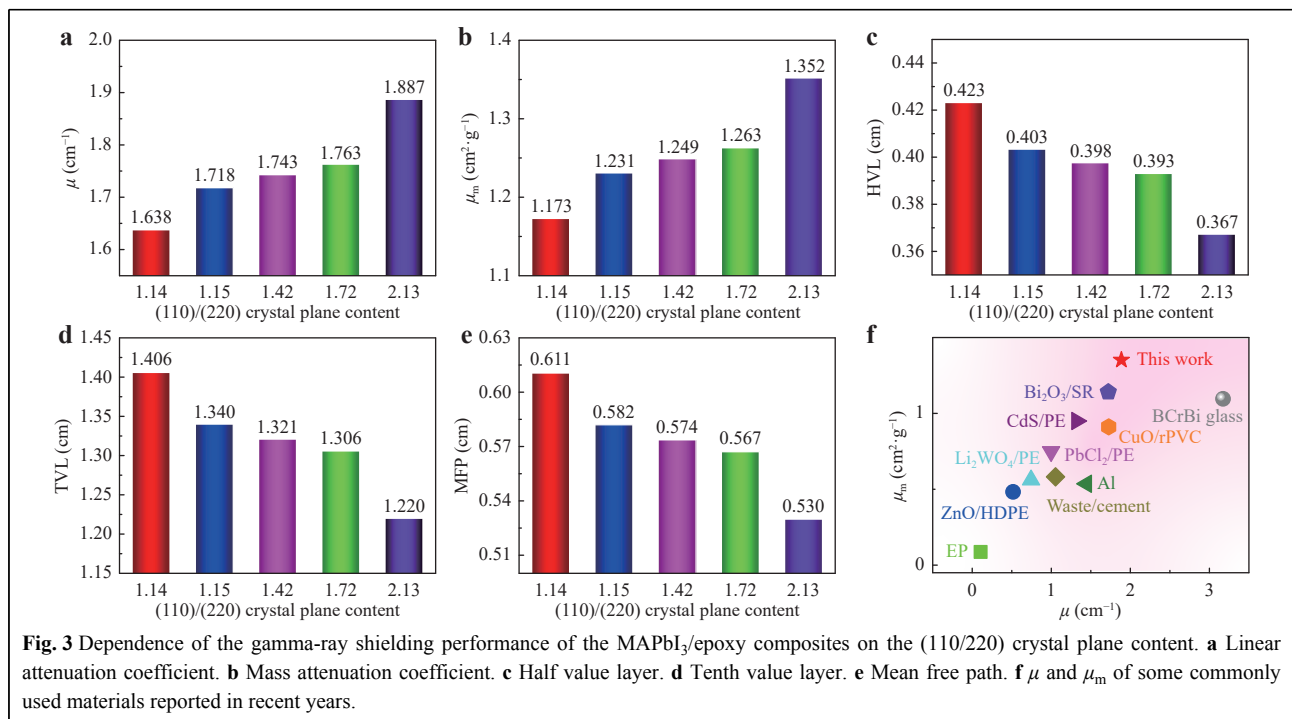
The gamma-ray shielding performance of the MAPbI₃/epoxy composites was explored by conducting narrow beam measurements using Am-241 as a radiation source of photons with an energy of 59.5 keV. During the measurement, the samples were placed in the same position between the collimator and detector. A NaI (TI) scintillation detector was employed to probe the intensity of gamma rays attenuated by the shielding materials.

The linear attenuation coefficients of the MAPbI₃/epoxy composites were measured and calculated using the Beer-Lambert law²⁸. As shown in Fig. 3a, the μ values of the MAPbI₃/epoxy composites were 1.638, 1.718, 1.743, 1.763, and 1.887 cm^{-1} , respectively, depending on the peak area ratios of the (110) plane to the (220) plane. The value of μ increased as this peak area ratio increased. This finding suggests that the high proportion of the (110) crystal plane contributes to the remarkable performance of MAPbI₃/epoxy composites. The dependence of the transmission (I/I_0) on the sample thickness is listed in

Table S1 for all samples.

As shown in Fig. 3b, similarly, the mass attenuation coefficients of the MAPbI₃/epoxy composites are dependent on the peak area ratios of the (110) plane to the (220) plane. The maximum mass attenuation coefficient was 1.352 $\text{cm}^2 \text{g}^{-1}$, which corresponds to a ratio of 2.13. This phenomenon again reveals that a high proportion of the (110) crystal plane is beneficial for the shielding performance of the MAPbI₃/epoxy composites because it facilitates collision with photons. Therefore, regulating the crystal planes of MAPbI₃ microcubic crystals can significantly enhance their shielding abilities. The μ values (0.106 cm^{-1}) and μ_m (0.087 $\text{cm}^2 \text{g}^{-1}$) of the pure epoxy are much lower than those of the MAPbI₃/epoxy composites, indicating that the introduction of MAPbI₃ can significantly improve the gamma-ray shielding performance of the epoxy.

In contrast, the HVL (half value layer), TVL (tenth value layer), and MFP (mean free path) of the MAPbI₃/epoxy composites decreased as the peak area ratio of the (110) plane to the (220) plane increased (Fig. 3c–e). The minimum values of HVL, TVL, and MFP were 0.367, 1.220, and 0.530 cm, respectively, corresponding to a ratio of 2.13. The smaller the HVL and TVL, the thinner the MAPbI₃/epoxy composite samples with substantial ability to attenuate gamma rays^{29,30}. For example, MAPbI₃/epoxy composite samples with a thickness of 36.7 mm of can attenuate half of the gamma rays with an energy of



59.5 keV, whereas MAPbI₃/epoxy composites with a thickness of 1.220 cm can attenuate as much as 90% of gamma rays. In addition, a smaller MFP indicates an increased probability of collision between the photons and MAPbI₃/epoxy composites in a certain volume³¹. In summary, these findings further confirm that the high shielding performance of MAPbI₃/epoxy composites is mainly attributed to the predominance of the (110) plane.

The μ and μ_m values of some commonly used shielding materials are shown in Fig. 3f^{32–39}. As can be seen, the current MAPbI₃/epoxy composites have superior gamma ray (59.5 keV) shielding ability, as indicated by their large μ and μ_m values relative to most of the commonly used shielding materials. The MAPbI₃/epoxy composites have higher μ values than most of those reported to date, indicating that the MAPbI₃/epoxy composites have a strong ability to attenuate gamma rays. Furthermore, the MAPbI₃/epoxy composites not only have excellent radiation attenuation ability but also have higher μ_m values. A higher μ_m value indicates that the MAPbI₃/epoxy composites have low density and lightweight characteristics, which make them suitable for a wider range of applications.

The gamma-ray shielding performance of the MAPbI₃/epoxy composites against Cs-137 (661 keV) and Co-60 (1250 keV) are presented in Table S2–S3. The radiation shielding performance of the MAPbI₃/epoxy composites is related to the photon energy of the gamma

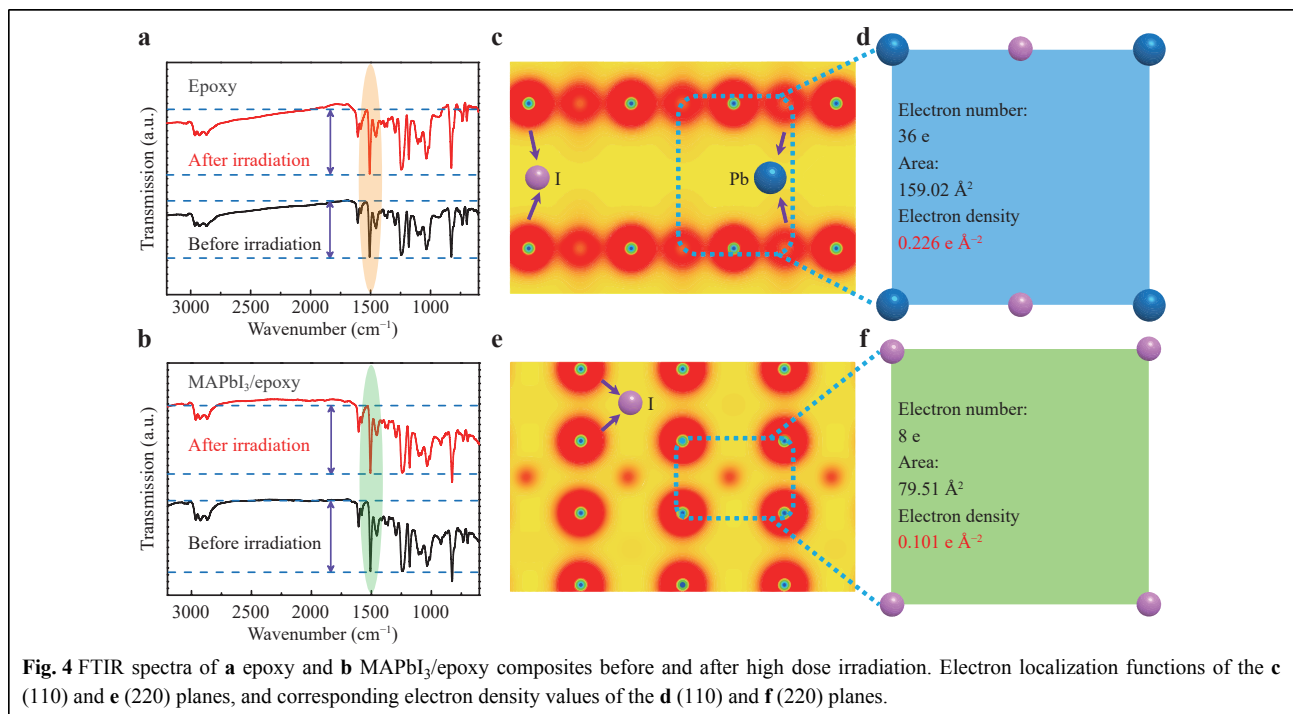
rays in that an increase in the photon energy lowers μ and μ_m . Furthermore, at higher photon energies, the crystal plane engineering strategy could also be successfully used to regulate the gamma-ray shielding performance.

Discussion

Irradiation stability and electron density

High-dose gamma-ray irradiation experiments on epoxy and MAPbI₃/epoxy composites were conducted to examine the transmission behaviour of incident gamma rays in the materials. The FTIR spectra (Fig. 4a, b) show that the intensity of the characteristic peaks of the epoxy at 1610, 1508, and 1294 cm⁻¹ increased significantly after high-dose irradiation, whereas the corresponding characteristic peaks of the MAPbI₃/epoxy composites underwent no obvious changes. This phenomenon indicates that the MAPbI₃/epoxy composites have excellent structural stability when exposed to high-dose irradiation.

To illustrate the modulation effects of the different crystal planes on the gamma-ray shielding ability, the electron localisation functions^{40,41} of the (110) and (220) planes were simulated using density functional theory (DFT) and the code of the Vienna *ab initio* simulation package (VASP)⁴². As shown in Fig. 4c, e, the electron localisation functions show that the electron density of the (110) plane originates from Pb and I in the ratio of one Pb atom to two I atoms. In contrast, the electron density of the



(220) plane originated only from the element I. These results suggest that the electron arrangement of the (110) plane is more compact than that of the (220) plane.

To estimate the electron density of the (110) and (220) planes, the area demarcated by the blue dotted line was selected. As shown in Fig. 4d, f, the electron density of the (110) plane is $0.226 \text{ e } \text{\AA}^{-2}$, which is larger than that of the (220) plane ($0.101 \text{ e } \text{\AA}^{-2}$), suggesting that the (110) plane provides more electrons for the incident photons to collide with. This indicates that the (110) plane can effectively attenuate the intensity of incident gamma rays. These findings reveal that crystal plane engineering is an effective strategy for the design of MAPbI₃/epoxy composites with excellent gamma-ray shielding performance. In addition to this, we measured the density of each MAPbI₃/epoxy composite, and the corresponding values are listed in Table S4. The densities of the MAPbI₃/epoxy composites was not influenced significantly by the content ratio of the (110) crystal plane to the (220) crystal plane, indicating that the crystal plane engineering strategy did not affect the gamma-ray shielding performance of MAPbI₃/epoxy composites by changing the material density.

Gamma ray shielding mechanism

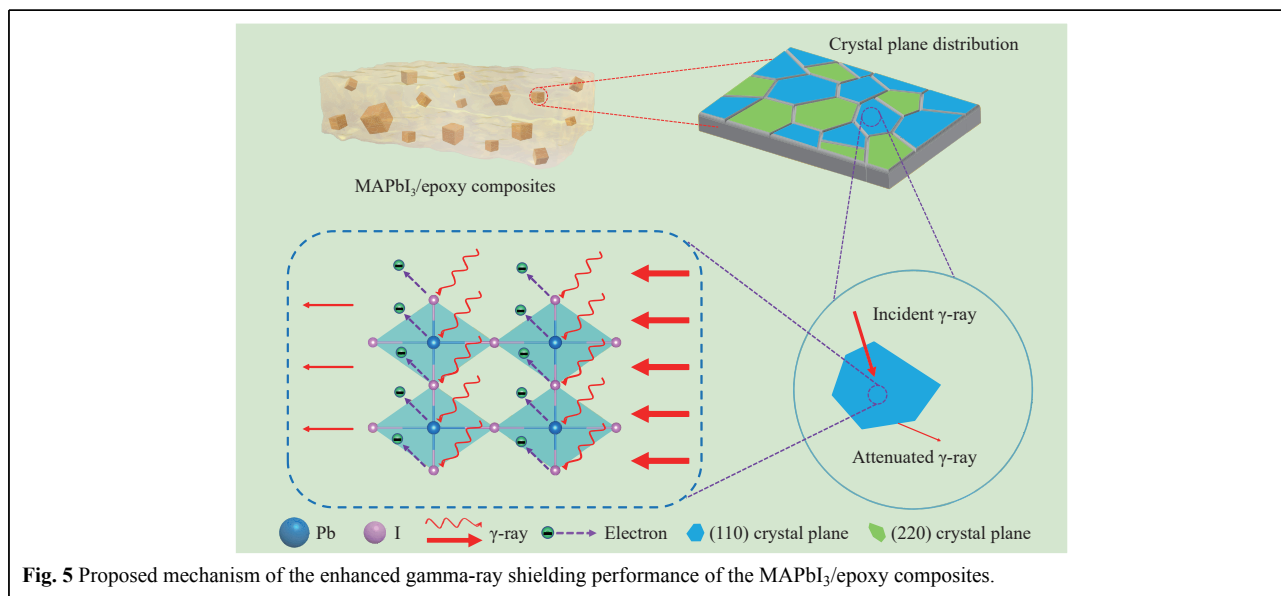
Based on the above results, we propose a mechanism whereby crystal plane engineering regulates the gamma-ray shielding performance of MAPbI₃/epoxy composites, as shown in Fig. 5. When gamma rays (59.5 keV) reach the MAPbI₃/epoxy composites, interaction between the incident gamma ray and the (110) plane or (220) plane induces the photoelectric effect. As a result, electrons are emitted, for which most of the energy of the gamma ray is

attenuated to overcome the electron binding energy in the L shell of Pb and the K shell of I⁴³.

As mentioned above, the electron density of the (110) plane is higher than that of the (220) plane. Therefore, it could be deduced that the attenuation of the incident gamma ray by the (110) plane is greater than that of the (220) plane because of the more effective collisions between the incident photons and extranuclear electrons. In other words, MAPbI₃/epoxy composites with more (110) planes exhibited improved gamma-ray shielding performance. In summary, crystal plane engineering is a useful strategy for the preparation of MAPbI₃/epoxy composites with the aim of enhancing the gamma-ray shielding performance by increasing the electron density.

Conclusion

In summary, based on the crystal plane engineering strategy, we prepared MAPbI₃ microcubic crystals with controllable electron density using a simple one-step solvothermal method. The experimental findings suggested that the gamma-ray shielding performance of MAPbI₃/epoxy composites is strongly correlated with the ratio of the peak area of the (110) plane to that of the (220) plane. The MAPbI₃/epoxy composite corresponding to the highest ratio of 2.13, exhibited a high linear attenuation coefficient (1.887 cm^{-1}) and a high mass attenuation coefficient ($1.352 \text{ cm}^2 \text{ g}^{-1}$). Crystal plane engineering was shown to be an effective strategy to effectively regulate the electron density of MAPbI₃/epoxy composites, thereby controlling the possibility of collision between the incident gamma rays and MAPbI₃/epoxy composites. The present work provides essential guidelines for the design and synthesis



of high-efficiency radiation-shielding materials.

Materials and methods

Materials

All chemicals were of analytical grade and used without further purification. Lead acetate ($\text{Pb}(\text{CH}_3\text{COO})_2$, 99.5%) and hydroiodic acid (HI, 48%) were acquired from Aladdin Biochemical Technology Co. Ltd. (China). Methylamine (CH_3NH_2 , 99%) and isopropyl alcohol ($(\text{CH}_3)_2\text{CHOH}$, 99.7%) were obtained from China Chemical Reagent Co., Ltd. Epoxy K-9761 was purchased from Guangdong Hengda New Material Technology Co. Ltd. (China).

Synthesis of MAPbI_3 microcubic crystals

A solvothermal method was used to synthesise the MAPbI_3 microcubic crystals. $\text{Pb}(\text{CH}_3\text{COO})_2$ powder (60 mg) and CH_3NH_2 (30 mL) were added to a mixture of HI (1 mL) and $(\text{CH}_3)_2\text{CHOH}$ (30 mL) under stirring for 30 min, after which the mixture was transferred to a 100 mL Teflon lined steel autoclave for the synthesis at 120 °C for a period of time (0.5, 1.0, 1.5, 2.0, 2.5 h). MAPbI_3 microcubic crystals were recovered by centrifugation and dried at 60 °C for 12 h.

Preparation of MAPbI_3 /epoxy composites

MAPbI_3 powder (20 wt. %) and epoxy resin were mixed by stirring for 5 min. The resulting mixture was poured into prefabricated PTFE moulds and left overnight at room temperature (22 ± 2 °C) for curing.

Characterisation

The crystallinity and phase purity of the samples were measured using an Empyrean X-ray diffractometer (PANalytical) with $\text{Cu } K_\alpha$ radiation ($\lambda = 1.541$ Å) at a scanning rate of 6° min^{-1} in the region of $2\theta = 10\text{--}80^\circ$. The particle size and morphology were determined using field emission scanning electron microscopy (FESEM, Carl Zeiss Company) with an accelerating voltage of 20 kV, and SEM-EDS was carried out using a Teneo volume scope. Fourier-transform infrared (FTIR) spectra were measured using a Thermo Nicolet iS50 spectrometer (Thermo Fisher Scientific). X-ray photoelectron spectroscopy (XPS) measurements were performed using a Thermo 250XI spectrometer (Thermo Fay). TEM and HRTEM measurements were performed using a Tecnai G2 F20 transmission electron microscope (FEI). Gamma irradiation experiments were carried out using the Co-60 radiation resource at the Heilongjiang Institute of Atomic Energy, China. The gamma-ray shielding performance of the MAPbI_3 /epoxy composites was evaluated using an Am-

241 source, and the transmittance was measured using an HD-2000 gamma-ray detector.

Details of density functional theory calculations

Our *ab initio* density functional theory calculations used projective enhancement waves to describe the core electrons and used the Perdew-Burke-Ernzerhof functional implemented in code of the VASP⁴² for generalised gradient approximation. We set an energy cutoff of 500 eV for the plane wave bases of all the systems to ensure an equal footing. All the calculations were performed at a convergence threshold of 10^{-4} eV. The energy relaxation at each strain step continued until the force on all the atoms converged to less than $0.02 \text{ eV } \text{Å}^{-1}$. The van der Waals interactions (vdW) were calculated using the DFT-D3 method. The stable (110) and (220) surfaces of MAPbI_3 were simulated using a slab model.

Calculations of gamma-ray shielding parameters

In a narrow beam measurement, the attenuated intensity of a gamma ray is a function of the thickness, expressed by the following equation²⁸:

$$I = I_0 \exp(-\mu x) \quad (1)$$

where I_0 is the intensity of the incident gamma rays, I is the intensity of the gamma rays passing through the shielding material, μ is the linear attenuation coefficient of the shielding material, and x is the thickness of the shielding material. μ represents the total interaction probability per unit thickness of the shielding material. During the experiments, the initial intensity and attenuated intensity of the gamma ray were measured, and then μ was calculated based on Eq. 1.

The mass attenuation coefficient is another useful parameter for evaluating the radiation-shielding performance of materials. Usually, μ_m is more meaningful than μ for the assessment of radiation-shielding materials. μ_m was calculated using Eq. 2⁴⁴:

$$\mu_m = \mu/\rho = \ln(I_0/I)/\rho x = \ln(I_0/I)/t_m = m \ln(I_0/I)/A \quad (2)$$

where ρ is the density of the shielding material (g cm^{-3}), t_m is the mass per unit area (g cm^{-2}), also known as the sample mass thickness, m is the mass of the material, and A is the surface area of the shielding material.

The half value layer (HVL) is a significant parameter. It is defined as the absorber thickness required to reduce the incident gamma-ray intensity to 50%. The HVL is calculated using Eq. 3²⁹:

$$\text{HVL} = X_{1/2} = (\ln 2)/\mu \quad (3)$$

where $X_{1/2}$ is the thickness of the shielding material required for the photon intensity to decay by half.

Similarly, the tenth layer (TVL) is defined as the absorber thickness required to lower the incident gamma-ray intensity to 10%. It is calculated using Eq. 4³⁰:

$$\text{TVL} = X_{1/10} = (\ln 10) / \mu \quad (4)$$

where $X_{1/10}$ represents the thickness of the shielding material required to attenuate the initial photon intensity by one-tenth.

Because the gamma rays interact with the shielding materials, the average distance that a photon travels between two successive interactions is known as the mean free path (MFP). The MFP is also referred to as the relaxation length (λ) and is calculated using Eq. 5⁴⁵:

$$\text{MFP} = \lambda = 1/\mu \quad (5)$$

Acknowledgements

Financial support provided by the National Natural Science Foundation of China (Grant No. U2067216), and NSAF (Grant No. U2130109) is greatly appreciated.

Author contributions

K.C. and Y.L. generated the original idea and designed the experiments. Q.Q.T. synthesised the samples. Q.Q.T. and W.J.W. performed experiments. K.C. and T.Y.Z. analysed the experimental data. K.C., J.Z.W. and H.J.K. wrote the manuscript. W.Q. and X.H.W. supervised experiments. The manuscript has been discussed and corrected by all authors.

Data availability

The data that support the plots in this paper and other findings of this study are available from the corresponding author upon reasonable request.

Conflict of interest

The authors declare that they have no conflict of interest.

Supplementary information is available for this paper at <https://doi.org/10.37188/lam.2022.051>.

Received: 24 June 2021 Revised: 03 November 2022 Accepted: 03 November 2022

Accepted article preview online: 08 November 2022

Published online: 08 December 2022

References

- Yu, G. B. et al. Moderate resolution imaging camera (MoRIC) of China's first Mars mission Tianwen-1. *Earth and Planetary Physics* **4**, 364-370 (2020).
- Durante, M. Space radiation protection: Destination Mars. *Life Sciences in Space Research* **1**, 2-9 (2014).
- Steffens, M. et al. Characterization of novel lightweight radiation shielding materials for space applications. *IEEE Transactions on Nuclear Science* **64**, 2325-2332 (2017).
- Eid, A. & Zawia, N. Consequences of lead exposure, and it's emerging role as an epigenetic modifier in the aging brain. *Neurotoxicology* **56**, 254-261 (2016).
- Ogawa, M. et al. Two cases of acute lead poisoning due to occupational exposure to lead. *Clinical Toxicology* **46**, 332-335 (2008).
- Hsiao, C. L., Wu, K. H. & Wan, K. S. Effects of environmental lead exposure on T-helper cell-specific cytokines in children. *Journal of Immunotoxicology* **8**, 284-287 (2011).
- Kim, J. H. Three principles for radiation safety: time, distance, and shielding. *The Korean Journal of Pain* **31**, 145-146 (2018).
- Wei, H. T. & Huang, J. S. Halide lead perovskites for ionizing radiation detection. *Nature Communications* **10**, 1066 (2019).
- Mahmoud, M. E. et al. Ceramic tiles doped with lead oxide nanoparticles: Their fabrication, physical, mechanical characteristics and γ -ray shielding performance. *Radiation Physics and Chemistry* **189**, 109780 (2021).
- Bagheri, K. et al. Thermal resistance, tensile properties, and gamma radiation shielding performance of unsaturated polyester/nanoclay/PbO composites. *Radiation Physics and Chemistry* **146**, 5-10 (2018).
- Aral, N., Banu, N. F. & Candan, C. An alternative X-ray shielding material based on coated textiles. *Textile Research Journal* **86**, 803-811 (2016).
- Aygün, H. H. & Alma, M. H. Bismuth (III) oxide/polyethylene terephthalate nanocomposite fiber coated polyester spunbonds for ionizing radiation protection. *Applied Physics A* **126**, 693 (2020).
- Prabhu, S., Bubbly, S. G. & Gudennavar, S. B. X-ray and γ -ray shielding efficiency of polymer composites: choice of fillers, effect of loading and filler size, photon energy and multifunctionality. *Polymer Reviews* <https://doi.org/10.1080/15583724.2022.2067867> (2022).
- Nambiar, S. & Yeow, J. T. W. Polymer-composite materials for radiation protection. *ACS Applied Materials & Interfaces* **4**, 5717-5726 (2012).
- Bijanu, A. et al. Metal-polymer composites for radiation protection: a review. *Journal of Polymer Research* **28**, 392 (2021).
- El-Khatib, A. M. et al. Gamma attenuation coefficients of nano cadmium oxide/high density polyethylene composites. *Scientific Reports* **9**, 16012 (2019).
- Yoo, J. J. et al. Efficient perovskite solar cells via improved carrier management. *Nature* **590**, 587-593 (2021).
- Kim, Y. H. et al. Comprehensive defect suppression in perovskite nanocrystals for high-efficiency light-emitting diodes. *Nature Photonics* **15**, 148-155 (2021).
- Liu, F. Y. et al. A rapid and robust light-and-solution-triggered in situ crafting of organic passivating membrane over metal halide perovskites for markedly improved stability and photocatalysis. *Nano Letters* **21**, 1643-1650 (2021).
- Li, Y. et al. Understanding the essential role of PbI_2 films in a high-performance lead halide perovskite photodetector. *The Journal of Physical Chemistry C* **124**, 15107-15114 (2020).
- Chen, Q. S. et al. All-inorganic perovskite nanocrystal scintillators. *Nature* **561**, 88-93 (2018).
- Wang, Y. et al. Amphoteric imidazole doping induced large-grained perovskite with reduced defect density for high performance inverted solar cells. *Solar Energy Materials and Solar Cells* **212**, 110553 (2020).
- Naphade, R. et al. Hybrid perovskite quantum nanostructures synthesized by electrospray antisolvent-solvent extraction and intercalation. *ACS Applied Materials & Interfaces* **8**, 854-861 (2016).
- Wang, Q. et al. Comparison of carrier dynamic behavior and photocatalytic molecular oxygen activation of optimized MAPbX_3 ($X = \text{I}, \text{Br}$). *Journal of Environmental Chemical Engineering* **8**, 104241 (2020).
- Holzer, H. & Dunand, D. C. Phase transformation and thermal expansion of $\text{Cu/ZrW}_2\text{O}_8$ metal matrix composites. *Journal of Materials Research* **14**, 780-789 (1999).
- Wang, S. H. et al. Accelerated degradation of methylammonium lead iodide perovskites induced by exposure to iodine vapour. *Nature Energy* **2**, 16195 (2017).
- Yang, M. J. et al. Square-centimeter solution-processed planar $\text{CH}_3\text{NH}_3\text{PbI}_3$ perovskite solar cells with efficiency exceeding 15%.

- Advanced Materials* **27**, 6363-6370 (2015).
28. Cao, D. et al. Gamma radiation shielding properties of poly (methyl methacrylate)/Bi₂O₃ composites. *Nuclear Engineering and Technology* **52**, 2613-2619 (2020).
 29. Waly, E. S. A., Fusco, M. A. & Bourham, M. A. Gamma-ray mass attenuation coefficient and half value layer factor of some oxide glass shielding materials. *Annals of Nuclear Energy* **96**, 26-30 (2016).
 30. Maksoud, M. I. A. A. et al. Gamma radiation shielding properties of poly(vinyl butyral)/Bi₂O₃@BaZrO₃ nanocomposites. *Materials Chemistry and Physics* **268**, 124728 (2021).
 31. Sayyed, M. I. Half value layer, mean free path and exposure buildup factor for tellurite glasses with different oxide compositions. *Journal of Alloys and Compounds* **695**, 3191-3197 (2017).
 32. Eid, M. S. et al. Implementation of waste silicate glass into composition of ordinary cement for radiation shielding applications. *Nuclear Engineering and Technology* **54**, 1456-1463 (2022).
 33. Alsayed, Z. et al. Investigation of γ -ray attenuation coefficients, effective atomic number and electron density for ZnO/HDPE composite. *Physica Scripta* **95**, 085301 (2020).
 34. Al-Hadeethi, Y. et al. Fabrication of lead free borate glasses modified by bismuth oxide for gamma ray protection applications. *Materials* **15**, 789 (2022).
 35. Abbas, M. I. et al. The influence of Bi₂O₃ nanoparticle content on the γ -ray interaction parameters of silicon rubber. *Polymers* **14**, 1048 (2022).
 36. Dilsiz, K. et al. Evaluation of CdS doped polyester composites regarding gamma and neutron shielding properties. *Progress in Nuclear Energy* **139**, 103865 (2021).
 37. Kaçal, M. R. et al. Analysis of radiation attenuation properties for Polyester/Li₂WO₄ composites. *Radiation Physics and Chemistry* **179**, 109257 (2021).
 38. Özkalaycı, F. et al. Lead(II) chloride effects on nuclear shielding capabilities of polymer composites. *Journal of Physics and Chemistry of Solids* **145**, 109543 (2020).
 39. El-Khatib, A. M. et al. Gamma radiation shielding properties of recycled polyvinyl chloride composites reinforced with micro/nano-structured PbO and CuO particles. *Physica Scripta* **96**, 125316 (2021).
 40. Xu, W. et al. Spectroscopic study and electronic structure of prototypical iron porphyrins and their μ -oxo-dimer derivatives with different functional configurations. *RSC Advances* **4**, 46399-46406 (2014).
 41. Meng, L. et al. Buckled silicene formation on Ir(111). *Nano Letters* **13**, 685-690 (2013).
 42. Kresse, G. & Hafner, J. *Ab initio* molecular dynamics for liquid metals. *Physical Review B* **47**, 558(R)-561(R) (1993).
 43. Xu, Q. et al. Visual clarity methylammonium lead trichloride perovskite single crystals for X and gamma rays protection. *Journal of Alloys and Compounds* **810**, 151896 (2019).
 44. Alim, B. et al. Experimental investigation of radiation shielding performances of some important AISI-coded stainless steels: Part I. *Radiation Physics and Chemistry* **166**, 108455 (2020).
 45. Sayyed, M. I. & Lakshminarayana, G. Structural, thermal, optical features and shielding parameters investigations of optical glasses for gamma radiation shielding and defense applications. *Journal of Non-Crystalline Solids* **487**, 53-59 (2018).